frontiers | Frontiers in Materials

TYPE Original Research
PUBLISHED 06 January 2023
DOI 10.3389/fmats.2022.1084999

OPEN ACCESS

EDITED BY
Cong Zhang,
Jiangnan University, China

REVIEWED BY
Amir R. Masoodi,
Ferdowsi University of Mashhad, Iran
Shao-Bo Kang,
Chongqing University, China

*CORRESPONDENCE
Yingbin Li,
281650659@qq.com

SPECIALTY SECTION
This article was submitted to Structural Materials, a section of the journal Frontiers in Materials

RECEIVED 31 October 2022
ACCEPTED 15 December 2022
PUBLISHED 06 January 2023

CITATION
Wang S, Li Y, Liu Z and Cheng T (2023), Calculation model of concrete-filled steel tube arch bridges based on the "arch effect".
Front. Mater. 9:1084999.
doi: 10.3389/fmats.2022.1084999

Calculation model of concrete-filled steel tube arch bridges based on the "arch effect"

Shaorui Wang, Yingbin Li*, Zengwu Liu and Tianlei Cheng

School of Civil Engineering, Chongqing Jiaotong University, Chongqing, China

In view of the limitations of the current code based on the equivalent beam-column method with the "rod mode" instead of the "arch mode" for the calculation of concrete-filled steel tube arch bridges, this paper takes the real bearing mechanism of the arch as the starting point and analyzes the different bearing mechanisms of the arch and eccentric pressurized column. The concrete-filled steel tube arch model test was carried out to analyze the deformation state and damage mode, and the geometric non-linear bending moment of the measured arch was compared with the bending moment value calculated by the eccentricity increase coefficient of the "rod mode." The results showed that the transfer of internal force is from the axial force to the arch axis, causing the vertical reaction force and horizontal thrust. However, the eccentric compression column only produced the vertical force at the bottom and combines with the lateral deformation indirectly generated by the eccentric distance. In addition, the deformation stage of the arch is basically the same as that of the eccentric compression column. The final failure mode of the arch is 4-hinge damage, and the final failure mode of the eccentric compression column is single-hinge damage. The preliminary geometric non-linear bending moment value obtained by the two modes accords well. Therefore, the main factors for the difference in the bearing mechanism between the two modes are different force structures, force transmission routes, and sources of deformation. Due to the difference in the bearing mechanism, the final failure mode is different, and the deformation ability of the arch is weakened by using the "rod mode" instead of the "arch mode." The geometric non-linear bending moment of the control section calculated by the eccentricity increase coefficient is conservative, but the influence of the geometric non-linearity of other sections is not considered enough.

KEYWORDS

concrete-filled steel tube arch, arch mode, geometric non-linearity, coefficient of eccentricity increase, equivalent beam and column method, eccentric compression column

1 Introduction

The concrete-filled steel tube (CFST) arch bridge having good span performance, superior bearing capacity, and graceful shape has been widely used. The CFST arch is restrained by the steel tube which significantly improves the compression resistance and spanning ability of the arch ribs, and the current braceless construction method of the arch bridge has matured, so the strong spanning ability, convenient construction method, and the ultra-high requirements for the foundation make the CFST arch bridge especially suitable for mountain and river canyons with treacherous terrain. However, large-span arch bridges are often affected by geometric non-linearity, and the damage rules are similar to those of eccentrically stressed columns (beam columns) due to the presence of both bending moments and axial forces in the arch cross-section. Therefore, the current specification (Ministry of Transport of the People's Republic of

China, 2015) usually equates the arch to a straight beam and column under eccentric compression for relevant calculation and takes the second-order effect of the arch into account by introducing the coefficient of the eccentricity increase coefficient to simplify the calculation. Although the eccentric compression column can basically reflect the failure law of the arch, the transverse deformation of the eccentric straight beam and column is produced by bending moment or transverse force. In contrast, the deformation of the arch is directly produced by the vertical load on the arch. The two deformation sources are different. In addition, the arch axis will generate additional internal forces including additional bending moments after compression. Also, the real internal forces of the arch are difficult to calculate, which is also different from the eccentrically compressed straight rod beam column (Chen, 2016). Therefore, several scholars have conducted the following relevant studies for the CFST arch structure with a special combination of forces:

Liu and Sun (2021) carried out six uniform load tests on CFST arches and studied the ultimate bearing capacity and deformation and failure characteristics of CFST round arch specimens. The results showed that the circular arch yields first at the inside of the arch foot, and the curvature at different positions of the specimen is no longer consistent. The steel tube at the arch foot will uplift obviously and the hoop action of the steel pipe on the concrete will fail when the CFST arches reach the ultimate bearing capacity. Li and Lei (2022) studied the influencing factors of the bearing capacity of CFST arches by numerical simulation and found that the arch had a great limitation on displacement in the elastic stage, and the ultimate bearing capacity was relatively high. The bearing capacity decreases obviously after reaching the peak value, but it showed good elongation performance. Zhao et al. (2021) used the fiber model technology to define the element bearing ratio by homogeneous generalized yield function and proposed the elastic modulus reduction method to evaluate the stable bearing capacity of the dumbbell-type CFST arch by strategically reducing the elastic modulus of the high-stress element. The results showed that stability had a significant impact on the CFST arch. The elastic modulus adjustment method has higher accuracy and efficiency than the incremental non-linear finite element method. Zhang et al. (2022) designed some concrete-filled steel tubular CFST columns and studied the influence of constraint effect coefficient and eccentricity on their mechanical properties. The results showed that the ultimate bearing capacity increases approximately linearly, and the ultimate deflection slightly decreases with the increase in the CFRP constraint effect coefficient. The ultimate bearing capacity of the specimen with large eccentricity decreases obviously, and the deflection corresponding to the ultimate bearing capacity is lower. Huo and Han (2014) compiled a program to analyze the non-linear behavior rules of five special-shaped arch bridges with their characteristics and revealed that the beam-column effect was the most critical factor affecting the essence of the arch and beam composite butterfly arch bridge. The non-linear method was used to calculate the tensile force of the cable by considering the vertical effect of the cable. Zou et al. (2023a) and Zou et al. (2023b) investigated composite and lattice web-concrete combination structures with hollow steel pipes and UHPC combinations and carried out load bearing tests on both combinations, and the results showed good load bearing performance, which can be used in pre-buried sections of CFST arch bridges to improve the load bearing capacity. Bradford and Pi (2014) investigated the effects of geometric non-linearity on the long-term in-plane performance of crown-pin CFST arches under the sustained central concentrated loading, and the analytical solutions for their non-linear response and buckling loads were derived, and the results showed that the long-term deformation predicted by the non-linear analysis resulted in a significant reduction in the serviceability limit state reserve of crown-pin CFST arches. Guo et al. (2022) deduced the calculation formula of the eccentricity increase coefficient based on the basic principle of the variational method and the interaction characteristics of the tie arch structure after deformation. The calculation results were compared with the finite element and the standard, and the results showed that the standard calculation results were large. The finite element calculation results were small, and the method calculation results adopted were moderate. Wang (2009) used the theory of the Updated Lagrangian (U.L.) finite element formulation, and the incremental equation of the virtual work of a three-dimensional (3D) beam for a geometric non-linear analysis of the space structure is established. The eccentric bearing capacity of CFST members is studied, and the results show that the larger the eccentric distance is, the lower the ultimate bearing capacity is, but with better ductility. Liu et al. (2011) and Wang and Guo (2020) studied the load carrying capacity and stability of a CFST arch bridge with fly-bird-type, calculated linear and non-linear stability coefficients, and analyzed the damage modes and load–displacement curves, and the results showed that the linear elastic buckling method does not reflect the true damage mode of this structure, and the effects of both geometric and material non-linearity cannot be ignored. Yang et al. (2020) proposed an adaptive strategy of the elastic modulus adjustment for the ultimate bearing capacity of the CFST arch, and the effectiveness of the method was proven by a large number of tests. Ye (2013) and Wu et al. (2015) studied the effects of length-to-slenderness ratio and sagittal-to-span ratio on the bearing capacity and suggested the essential difference between the arch and column. Wei et al. (2010), Wei et al. (2009), and Chen et al. (2004) used the equivalent beam-column method to calculate the ultimate bearing capacity of the CFST parabolic arch, and the comparison results with finite elements showed that this method is more accurate. Yuan et al. (2020), Jiang et al. (2018), and Zhang and Yu (2013) studied the out-of-plane stability of CFST arches, explored the effect of non-linearity on the stability coefficients, and proposed a method for calculating the correlation coefficients for stability calculations. Bradford and Pi (2014) investigated the effects of geometric non-linearity on the long-term in-plane behavior of crown-pinned circular CFST arches under a continuous central concentrated load and showed that geometric non-linearity has a significant effect on the long-term behavior of crown-pinned CFST arches.

The research on the ultimate bearing capacity and the eccentricity increase coefficient of the CFST arch is abundant, but the research foundation is still built based on the ideas of the "rod mode." The research on the calculation pattern of the CFST arch based on the "arch effect" is deficient. In view of this, this paper discussed the differences between the bearing mechanism of the "arch mode" and the "rod mode" and proposed a new calculation model for the real geometric non-linear internal forces of the arch after force deformation. In this paper, we carried out model tests on the single-pipe arch of steel pipe concrete; analyzed the load–displacement curves, strains, and damage modes of the whole process damage of two single-point loading conditions; and verified the difference between the "arch mode" and "rod mode" damage modes. The comparison of model test and regulation was based on the equivalent beam-column method for non-linear bending moments in arch geometry, and

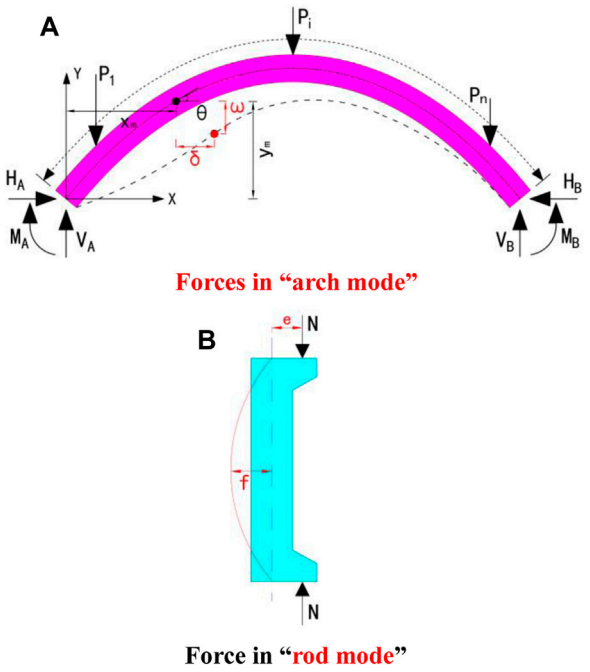

FIGURE 1
Stress characteristics of the "arch mode" and "rod mode": **(A)** Forces in "arch mode"; **(B)** Force in "rod mode".

the analysis of the differences between the two calculation results and the advantages of the calculation mode was carried out based on the arch effect. The regulation of using the "rod mode" instead of the "arch mode" in the calculation of CFST arch bridges is discussed. Based on the differences of the two modes in the bearing mechanism, this paper proposes the real internal force calculation mode of each section after the deformation of the arch. The mode provided new ideas for the future calculation mode of the bearing capacity and stability of large-span arch bridges. Also, it can help optimize the arch axis, arch rib section form, and structure.

2 The bearing mechanism of the "arch mode"

If the branch buckling mode of the unhinged arch is anti-symmetric, as shown in Figure 1A, the horizontal thrust will be generated at the support, and the axial pressure will be generated in the section under the vertical load of the arch. Therefore, the actual internal force of any section can be calculated as Formula 1, after the arch deformation reaches a new equilibrium state.

$$M_g = M_A + V_A(x_m + \delta) - H_A(y_m - \omega) - \sum P(x_m - x_{pi}). \quad (1)$$

According to the theory of deflection, the calculation of the axial force in the arch section can be expressed approximately as

$$N_g = \frac{H_A}{\cos\theta} = \frac{V_A - \sum P_i}{\sin\theta}. \quad (2)$$

Type: M_g—real bending moment of any section of the arch; N_g—arch section axial force; θ—angle between the tangent line and horizontal direction at any position of the arch axis; M_A—arch foot bending moment; V_A—vertical reaction of the arch foot; H_A—horizontal reaction of the arch foot; x_m—x coordinate of section; y_m—y coordinate of the section; δ—horizontal displacement of the section; ω—vertical displacement of the section; P_i—acting external load on the arch; x_{pi}—x coordinate of the external load P_i.

It is not difficult to see that the presence of the horizontal thrust reduces the bending moment in the arch, and the arch axis will produce additional internal forces including the additional bending moment after compression under the action of pressure, which is $\Delta M_g = N_g \omega \cos\theta$.Therefore, the bearing mechanism of the unhinged arch can be summarized as follows: under the action of external load, the axial force in the arch is transferred to the arch foot through the arch axis, generating horizontal thrust and vertical reaction force at the arch foot, and the external load directly produces deformation. In the new equilibrium state after deformation, the section bending moment is mainly composed of the linear bending moment, which is $M_r = M_A + V_A x_m - H_A y_m - \sum P_i(x_m - x_{pi})$ and the non-linear bending moment, which is $\Delta M_r = V_A \delta + H_A \omega$. The axial force is not affected by non-linearity. Therefore, the failure of the bearing capacity of the arch mainly comes from the linear bending moment generated by the internal force of the arch foot and the external load and the non-linear bending moment directly generated by the external load.

However, based on the principle of the equivalent beam-column method, the current domestic standard equates the arch ring to a simply supported eccentric compression column with a length of .36 S (S is the arc length of the arch axis), as shown in Figure 1B (Lin and Chen, 2016). The internal force of the section is as follows:

$$M_c = N(e + f), \quad (3)$$

$$N_c = N. \quad (4)$$

Type: M_c—real bending moment of the eccentric compression column section; N_c—eccentric compression column axial force N—eccentric force; e—Eccentricity, and f—transverse deformation of the cross section.

It can be found from the analysis of the real internal force of the eccentric compression column that the eccentric force transfer to the fixed end along the axis directly forms the vertical reaction force. The axial force is equal to the eccentric force. The cross-section bending moment is produced by the eccentricity, and thus it indirectly leads to lateral deformation. So, the bearing capacity of eccentric compression column destruction mainly comes from the vertical force produced by the linear bending moment and transverse deformation and eccentricity of the additional bending moment.

In view of the differences in the bearing mechanisms of the "arch mode" and "rod mode," the load-bearing capacity model test of the CFST single-pipe arch was carried out from the real force mode of the arch. By analyzing the load–displacement state, the damage mode and the real internal force in the arch in the geometrically non-linear stage, the difference between the "arch mode" and "rod mode" is verified, and a new calculation model of the CFST arch bridge based on the arch effect is proposed.

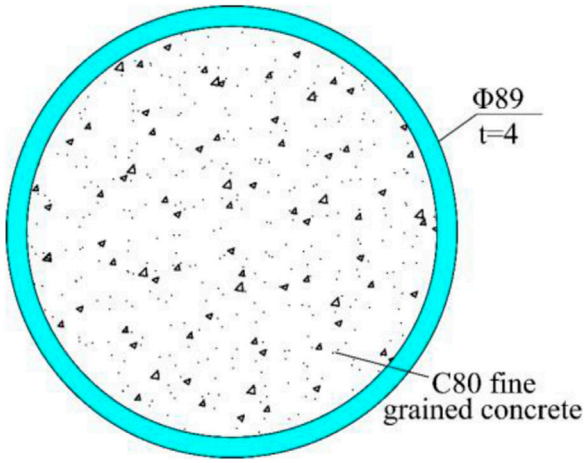

FIGURE 2
Cross-section of the arch rib.

3 Single-tube model test of the "arch mode"

3.1 Model design and production

A catenary steel tube single-tube arch bridge with a calculated span of 95 m was used as the prototype. The ratio of the sagittal span was 1/3.5, the calculated sagittal height was 27.143 m, the arch axis coefficient was 1.5, the diameter of the steel tube was 1.55 m, the wall thickness of the arch foot was 26 mm, and the rest was 22 mm, and C60 concrete was poured into the tube.

The test arch was scaled down at 1:16, with a reduced span of 5.938 m and a calculated height of 1.696 m. Due to the limitation of market steel pipe specifications, the pipe wall was too thin according to the actual scale ratio, so the full-span diameter and wall thickness of the steel pipe were set at 89 mm and 4 mm, respectively, according to the existing market specifications, as shown in Figure 2. Scale parameters and scale deviation values are shown in Tables 1, 2.

The steel pipe material was Q345, and the arch was perfused with C80 fine-grain concrete. After curing for 28 days, the compressive strength of six concrete blocks was tested. The compressive strength of the cube was 51.85 MPa, the compressive strength of the prismatic core was 32.4 MPa, and the elastic modulus was 3.4834×10^4 MPa. Steel tube yield strength was 361 MPa, tensile strength was 540 MPa, and the elastic modulus was 2.1×10^5 MPa.

The vault and L/4 loading conditions were designed to test the in-plane deformation state, strain distribution, and failure mode of the whole process of the arch. The overall design is shown in Figure 3.

3.2 Designs of the test device and measuring point

A 50-t hydraulic jack was adopted. The top of the jack was a pressure sensor, and the bottom design disk was in contact with the arch rib loading block to ensure uniform force. The skewback reaction device was a triangular steel structure. The test was mainly conducted to study the load bearing capacity of the arch under vertical load in-plane deformation. In order to avoid out-of-plane deformation causing out-of-plane instability damage to the structure, the whole arch set five transverse limits to ensure that the arch was only in-plane free deformation during the loading process. The contact surface between the limit and the arch was coated with a tetrafluoro plate to reduce friction. The main device configuration is shown in Figure 3 and Figure 4A. Percentage gauges and strain gauges were used to test the displacement and strain in the whole process. Two percentage gauges were set at each L/8 to measure the horizontal and vertical displacement, and four percentage gauges were set at each skewback to monitor whether deflection occurred, as shown in Figure 4B. Strain gauges are set at the L/8 and the section of the two arch feet. The upper and lower edges of the section are arranged in annular and longitudinal directions, respectively, while only longitudinal directions are arranged on the side. Fifty-four strain gauges are arranged in the whole arch, as shown in Figure 5.

TABLE 1 Parameters of the scaled section.

Project	Span (m)	Rise (m)	String pipe diameter (m)	Wall thickness (m)	Inner diameter of chords (m)
Original bridge	95	27.143	1.55	.026	1.498
Ideal scale value	5.938	1.696	.0969	.00163	.09364
Actual scale value	5.938	1.696	.089	.004	.081

TABLE 2 Scale size deviation.

Project	Ideal scale value	Actual scale value	Percentage deviation (%)
Area (m^2)	.00048786	.00106814	118.95
In-plane moment of inertia (m^4)	5.5366E-07	9.67E-07	74.62
Compressive stiffness (N/m)	100498797	220037149	118.95
Bending stiffness ($N{\cdot}m^2$)	114053.946	199161.125	74.62

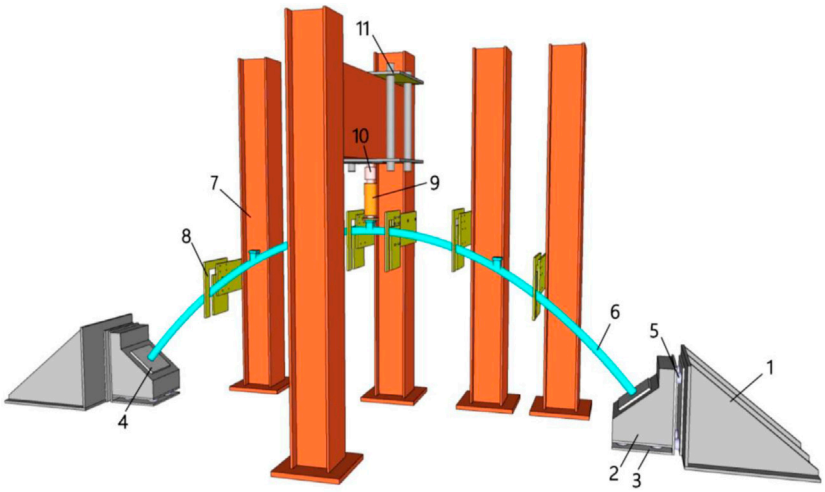

1—Skewback reaction tower; 2—Skewback; 3—Skewback bearing plate; 4—Skewback embedded parts; 5—Skewback pressure sensor; 6—Arch; 7—Pillar; 8—Lateral limit; 9—Jack; 10—Jack pressure sensor; 11—Jack reaction frame;

FIGURE 3
Overall diagram of the model.

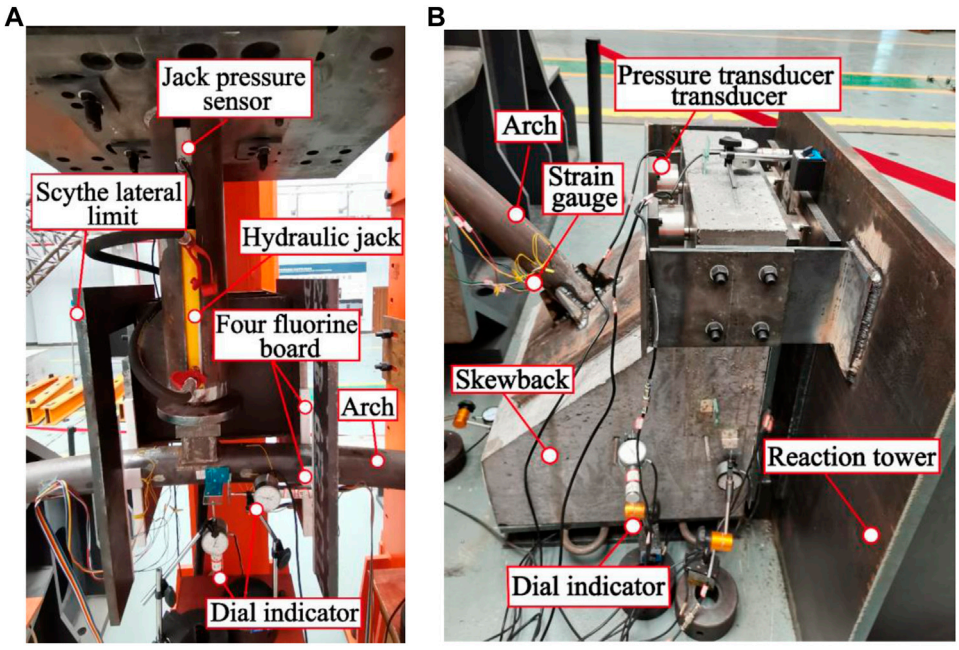

Main test equipment **Structural diagram of the skewback**

FIGURE 4
Real diagram of local construction: **(A)** Main test equipment; **(B)** Structural diagram of the skewback.

3.3 Measurement method for internal force

According to Eq. 1, the real internal forces of any section can be calculated if the internal forces of the arch foot, section displacement, and external load are known, based on the calculation principle of the real internal forces in the arch. The section displacement and external load can be directly measured by the test, while the actual measurement of the internal forces of the arch foot is difficult to measure. In this paper, the separation skewback method in Li (2012) was used to measure the internal force of the arch foot. Four sensors were installed on the back and bottom of the skewback to measure the horizontal thrust and

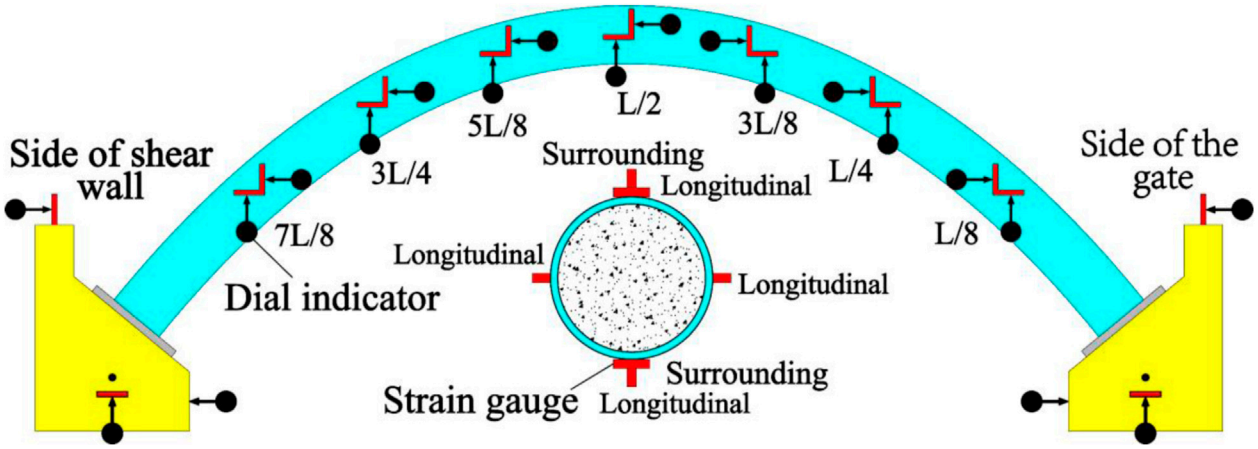

FIGURE 5
Placement of displacement and strain measurement points.

FIGURE 6
Four-point loading skewback.

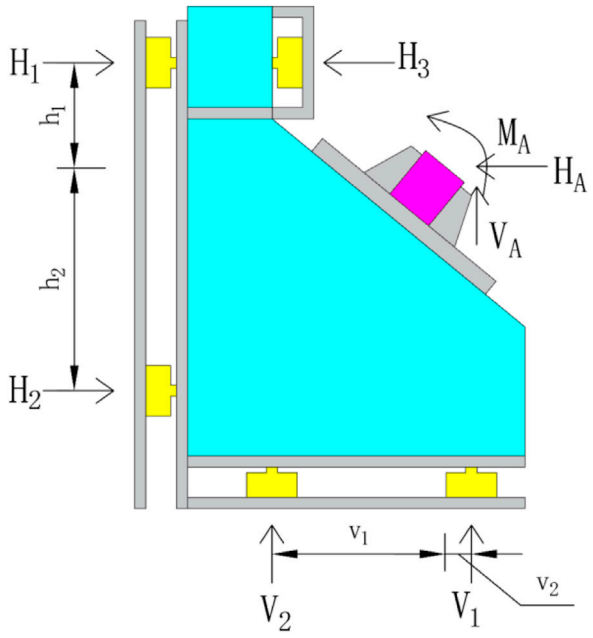

FIGURE 7
Schematic diagram of calculation of the internal force of the arch foot.

vertical reaction force, as shown in Figure 8. Due to the effect of the arch foot bending moment, the skewback will have a trend of in-plane rotation. It was found in finite element analysis that the arch foot at both ends of the vault loading has a negative bending moment, and the skewback rotates clockwise. In four-point loading, there is a negative bending moment at the arch foot close to the loading point, and the skewback rotates clockwise, while there is a positive bending moment at the arch foot far away from the loading point, and the skewback rotates counterclockwise. To accurately measure the horizontal thrust of the arch foot and limit the rotation of the skewback, two sensors are set at the front of the top of the vault loading base (Figure 4B). Two sensors are set at the front of the top and the front of the bottom of the skewback near and far from the loading point of the four-point loading (Figure 6; Figure 4B). Then, the bending moment, horizontal reaction force, and vertical reaction force of the arch foot are calculated according to the static equivalence principle. The calculation principle is shown in Figure 7.

Through force analysis, the actual calculation formula of the arch foot bending moment, horizontal reaction force, and vertical reaction force can be obtained as follows:

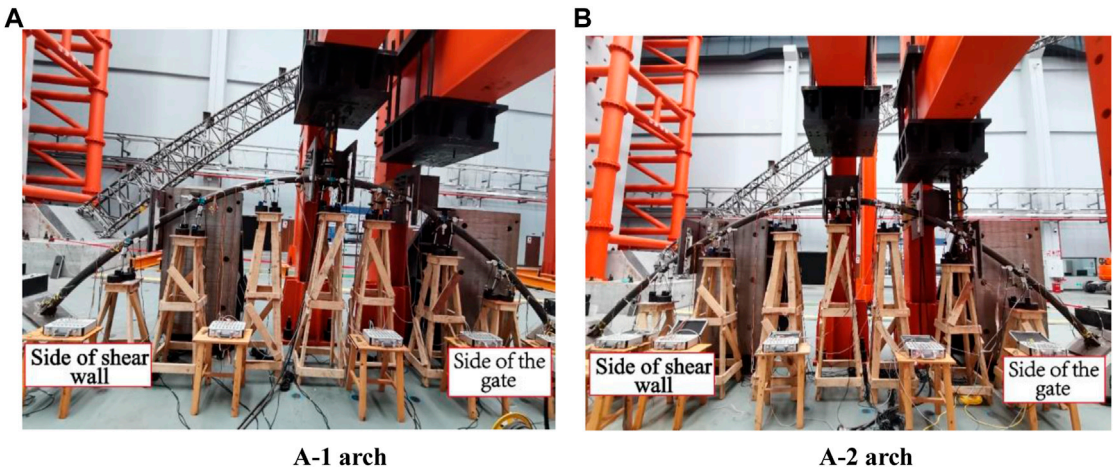

FIGURE 8
Initial state: **(A)** A-1 arch; **(B)** A-2 arch.

TABLE 3 Hierarchical loading value (Unit: kN).

Vault loading condition				Quarter section loading condition			
Classification	Load value	Classification	Load value	Classification	Load value	Classification	Load value
1	.500	11	30.891	1	.400	11	24.713
2	1.000	12	35.891	2	.800	12	28.713
3	1.750	13	40.891	3	1.400	13	32.713
4	2.875	14	45.891	4	2.300	14	36.713
5	4.563	15	50.891	5	3.650	15	40.713
6	7.094	16	55.891	6	5.675	16	44.713
7	10.891	17	60.891	7	8.713	17	48.713
8	15.891	18	63.391	8	12.713	18	50.713
9	20.891	19	64.641	9	16.713	19	50.838
10	25.891	20	65.266	10	20.713	—	—

$$\begin{cases} H_A = H_1 + H_2 - H_3 \\ V_A = V_1 + V_2 \\ M_A = H_1 h_1 - H_2 h_2 - H_3 h_3 - \\ \qquad V_1 v_1 + V_2 v_2 \end{cases} \cdot \tag{5}$$

Type: H_A—horizontal reaction force; H_1, H_2, H_3—net force value of each drainage smooth reaction force sensor; h_1, h_2, h_3—vertical distance from each drainage reaction sensor to the center of the arch foot; V_1, V_2—net force value of each row of the vertical reaction sensor; v_1, v_2—horizontal distance from each row of vertical reaction sensors to the center of the arch foot.

3.4 Test steps

First, the reaction tower and skewback should be precisely positioned. It was necessary to pre-push it to eliminate the anchor hole clearance after the reaction tower was installed. Then, the arch ribs were erected and the hanging hammer was used to ensure that the arch was in a vertical state without initial transverse deviation. Finally, the loading device and test device are installed. The initial state after the preparation is shown in Figure 8. Formal loading needs to be graded according to the results of finite element ultimate bearing capacity analysis, that is, the ultimate force of 0%–3% or so average .5 kN/level, 3%–5% or so average 1 kN/level, 5%–10% or so average 2 kN/level, and 10% after the average 5 kN/level until failure, with each

TABLE 4 Description of working conditions.

Model number	Loading condition
A-1	Vault loading condition
A-2	Quarter section loading condition

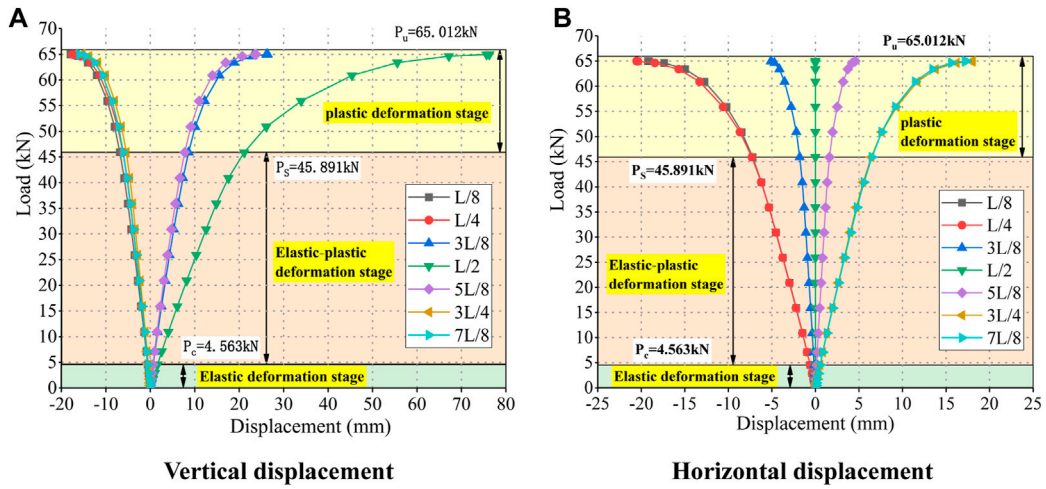

FIGURE 9
A-1 arch of the load–displacement curve: **(A)** Vertical displacement; **(B)** Horizontal displacement.

static loading level of 2 min after the stability of the reading. Full-arch graded loading values are shown in Table 3. The test designed two loading conditions. The arch top loading arch rib was named A-1 and 4-point loading condition arch rib was named A-2. The description of the conditions is given in Table 4 and the actual loading figure is shown in Figure 8.

3.5 Analysis of test results

3.5.1 Load–displacement curve

According to Table 3, the load–displacement curves of each section of the A-1 arch and A-2 arch are shown in Figures 9, 10 (vertical displacement is "+" downward and horizontal displacement direction of shear wall side arch is "+"). The whole deformation process of the arch can be roughly divided into three stages:

(1) Elastic deformation stage. When the A-1 arch was loaded to 4.563 kN (.07 P_u) and the A-2 arch was loaded to 3.65 kN (.073 P_u), the load–displacement curves of each section basically changed linearly, and the arch was in the stage of linear elastic change, almost unaffected by non-linear influence.
(2) Elastic–plastic deformation stage. With the increase in the load, the slope of the curve gradually decreases, and the arch enters the stage of elastic–plastic deformation. The sections, especially the sections at loading points, are gradually affected by geometric non-linearity. At this stage, the upper critical load limit for arch A-1 was about 45.891 kN (.71 P_u), and the upper critical load limit for arch A-2 was about 40.713 kN (.81 P_u).
(3) Plastic deformation stage. With the increase in the load, the deflection of the loading point increases continuously, the slope of the curve increases faster, and the curve gradually tends to be horizontal. Under the double non-linear action, the arch has a slight change in load, a sharp increase in displacement, and a reduction in load value. The load could not be increased continuously when the A-1 and A-2 arches were added to 65.012 kN and 50.275 kN, respectively.

The results of failure load–displacement curves under two working conditions showed that the ultimate bearing capacity of the A-1 arch was P_u = 65.012 kN, the maximum vertical displacement of the loading point was 76.31 mm, and the maximum horizontal displacement of the L/4 section was 20.53 mm. The ultimate bearing capacity of the A-2 arch was P_u = 50.275 kN, and the maximum vertical displacement and horizontal displacement of the loading point are 108.96 mm and 84.96 mm, respectively. The comparison between the test results under the ultimate load and the preliminary FEM calculation is shown in Table 5. The comparison results showed that the difference between the test ultimate bearing capacity value and the preliminary calculation was less than 2%, and the displacement difference was about 10%. It indicated that the ultimate bearing capacity test values of the two working conditions are accurate. The real CFST arch shows superior deformation capacity compared with the theoretical calculation.

3.5.2 The strain state under ultimate load

All steel tube surfaces in L/8 and two arch feet were decorated with a strain gauge, as shown in Figure 5. As the deformation of the test arch was mainly in-plane deformation, only the edge of the steel tube on the longitudinal strain under the ultimate load was analyzed. It is given in Section 3.1 that the measured yield strength of the steel pipe was 361 MPa, the modulus of elasticity was 2.1 × 10^5 MPa, and the steel pipe yield strain was $\varepsilon_y = \sigma_y/E = 1719$. The whole arch strain and tube concrete crack distribution are shown in Figure 11. The positive direction of the transverse coordinate axis indicates gate side arch seat to shear wall side arch seat. The specific analysis of concrete cracks will be shown in the next section. The strain distribution results showed that the steel pipe at the location

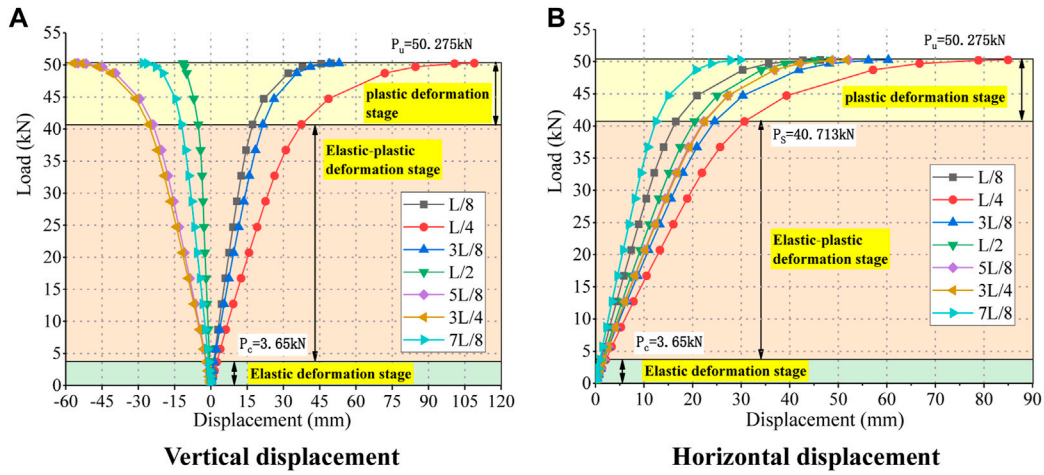

FIGURE 10
A-2 arch of the load–displacement curve: **(A)** Vertical displacement; **(B)** Horizontal displacement.

TABLE 5 Comparison between the test value and preliminary calculated value of the ultimate load.

Category	A-1 arch			A-2 arch		
	Test result	Preliminary calculated value	Percentage of difference	Test result	Preliminary calculated value	Percentage of difference
Ultimate bearing capacity (kN)	65.012	65.266	−.39%	50.275	50.838	−1.11%
Maximum vertical displacement (mm)	76.31	69.53	9.75%	108.96	96.31	13.13%
Maximum horizontal displacement (mm)	20.53	19.02	7.94%	−84.96	−75.73	12.19%

where the concrete cracks appear had yielded. The tensile and compressive strain values of the upper and lower edges of the steel pipe were basically symmetric, and the strain at the upper and lower edges of the loading site reached the peak. The strain distribution and the location of cracks corresponded with each other.

3.5.3 Damage state

The initial state of two loading conditions and the overall deformation state under the ultimate load are shown in Figure 12. The concrete in the tube after destruction is shown in Figure 13.

It can be seen that the vault has obvious vertical sag in the ultimate state of the bearing capacity of the A-1 arch. There are several small vertical micro-cracks perpendicular to the arch axis extending upward to the lower edge of the concrete in a certain area at both ends of the loading point. There was an obvious bulge near the L/4 section, and a macroscopic crack on the upper edge of the concrete extends downward perpendicular to the axis of the arch. There was a slight depression near the cross-section of the two arch feet, and a macroscopic crack on the lower edge of the concrete extends upward perpendicular to the axis of the arch.

In the ultimate state of the bearing capacity of the A-2 arch, the L/4 section was inclined to sag, and there was a macroscopic crack at the lower edge of the concrete perpendicular to the arch axis extending upward. The arch foot section of the gate side was slightly raised, and there was a macroscopic crack on the upper edge of the concrete that was perpendicular to the arch axis extending downward. There was an obvious bulge near the 3L/4 section, and a macroscopic crack on the upper edge of the concrete extends downward perpendicular to the axis of the arch. There was a slight depression near the section of the arch foot on the shear wall side, and a macroscopic crack at the lower edge of the concrete extends upward perpendicular to the arch axis.

Combined with Figure 10 and the aforementioned failure states, it can be seen that the four crack positions of the concrete in the tube after failure under the two working conditions all appear near the extreme point of the tensile strain of the steel tube, which was a tensile failure. At this time, the concrete at the crack stops working, indicating that plastic hinges are formed at the four positions in the arch and that the structure cannot continue to bear. Therefore, the failure mode of the arch was the 4-hinge failure, and the structure forms a geometrically variable system and loses the bearing capacity.

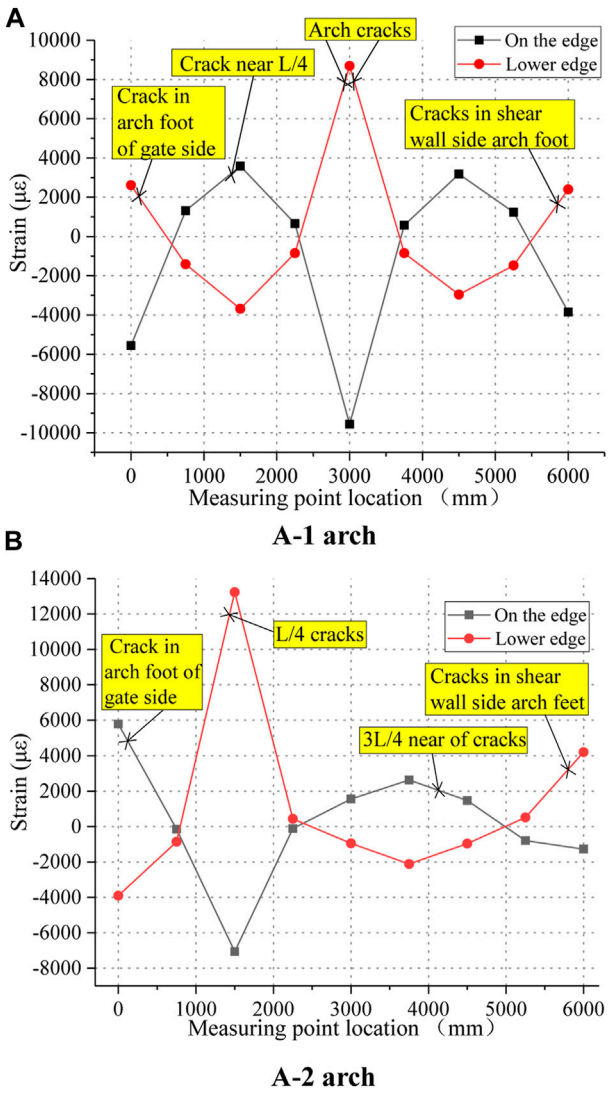

FIGURE 11
Strain and crack distribution of concrete in the tube under ultimate load: **(A)** A-1 arch; **(B)** A-2 arch.

4 Comparative analysis of the "arch mode" and "rod mode"

In Section 3.5.1, the loading interval of the A-1 arch with obvious geometric non-linearity is given as 4.563 kN–45.891 kN, and that of the A-2 arch is 3.65 kN–40.713 kN. The calculation section of the A-1 and A-2 arches and the selection of loads outside the geometric non-linear loading interval are listed in Table 6. The geometric non-linear bending moment values of the two calculation modes are compared under the corresponding external load.

4.1 Calculated geometric non-linear bending moment values for the regulation

In the current JTG/TD65-06-2015 code (concrete-filled steel tube arch bridge design code) (Ministry of Transport of the People's Republic of China, 2015), the eccentricity increasing coefficient η is introduced into the calculation formula of the ultimate bearing capacity of the CFST arch to consider the geometric non-linearity of the arch. The main parameters of the formula are the Euler critical force formula and first-order linear axial force, as shown in Eq. 6. It can be seen that the arch is equivalent to an eccentric compression column for calculation based on the equivalent beam-column method in the arch bridge specification. Its essence is that the first-order bending moment obtained by elastic calculation is enlarged by the eccentricity increasing coefficient, which is equal to the moment existing in the control section of the actual component. Then, the geometric non-linear bending moment is calculated, as shown in Eq. 7.

$$\eta = \frac{1}{1 - 0.4N/N_E}, \tag{6}$$

$$M' = \eta M. \tag{7}$$

Type: η—eccentricity increase coefficient; Euler critical force $N_E = \frac{\pi^2 E_{sc} A_{sc}}{\lambda^2}$, of which, E_{sc}—combined the elastic modulus of CFST, A_{sc}—combined the cross-sectional area of CFST; N—first-order linear axial force, M'—geometric non-linear bending moment, and M—linear bending moment.

According to the section-related parameters of the test arch provided in Section 3.1, the Eulerian critical force N_E = 304.3 kN can be calculated. The first-order linear axial force and bending moment can be calculated by finite elements as recommended in the regulation. So, the first-order linear axial force and bending moment of the test arch were calculated by Midas/civil, as shown in Table 7.

The Eulerian critical force and the first-order axial force and bending moment values corresponding to the external loads P_1~P_4 in Table 7 are substituted into Eqs 6, 7, obtaining the eccentricity increasing coefficient η and geometric non-linear bending moment values M' of the corresponding sections, as shown in Table 8.

4.2 Measured geometric non-linear bending moment values based on the arch effect calculation model

According to the geometric non-linear internal force calculation model based on the arch effect proposed in this paper according to Eq. (1), the real geometric non-linear bending moment in the arch can be calculated by substituting the measured load–displacement results and the coordinate position of the cross-section. The cross-section positions and the measured external loads P_1~P_4 correspond to the horizontal displacement δ and vertical displacement ω (arch foot displacement is 0), as shown in Tables 9, 10.

The measured values of horizontal thrust H_A, vertical reaction V_A, bending moment M_A, and other cross-section geometric non-linear bending moment values M_g in the arch foot of the gate side are shown in Table 11.

4.3 Comparative analysis

The geometric non-linear moment values calculated by the regulation in Table 8 are compared with the real geometric non-linear moment values of the CFST arch measured in Table 11, as shown in Table 12 and Figure 14.

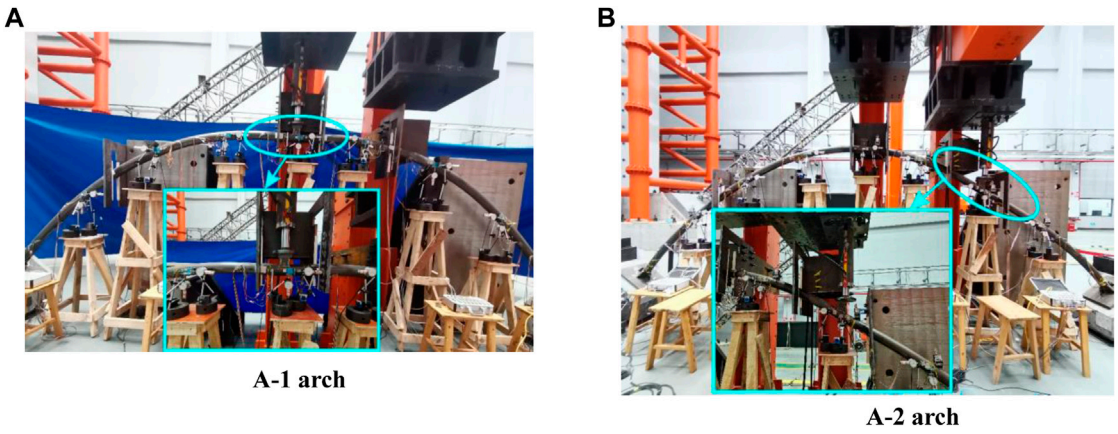

FIGURE 12
State after destruction: **(A)** A-1 arch; **(B)** A-2 arch.

TABLE 6 Selection of calculation parameters.

Condition	Calculate the cross section			Loading (kN)			
				P_1	P_2	P_3	P_4
A-1	Arch foot	L/4	Vault	15.891	25.891	35.891	45.891
A-2	Arch foot	L/4	3L/4	16.713	24.713	32.713	40.713

TABLE 7 First-order linear axial forces (N) and bending moments (M) calculated by finite elements.

Condition	P_1		P_2		P_3		P_4	
	N (kN)	M (kN·m)	N (kN)	M (kN·m)	N (kN)	M (kN·m)	N (kN)	M (kN·m)
A-1	14.246	2.825	23.211	4.602	32.177	6.38	41.142	8.157
	14.969	−1.849	24.389	−3.012	33.809	−4.176	43.229	−5.339
	12.879	4.845	20.984	7.893	29.089	10.942	37.193	13.991
A-2	15.789	−4.41	23.346	−6.521	30.904	−8.632	38.462	−10.742
	5.615	6.024	8.302	8.908	10.99	11.792	13.677	14.675
	8.28	−2.185	12.243	−3.231	16.206	−4.276	20.17	−5.322

TABLE 8 Geometric non-linear bending moment values calculated by the regulation (unit: kN).

Condition	Cross-section position	P_1		P_2		P_3		P_4	
		η	M'	η	M'	η	M'	η	M'
A-1	Gate-side arch foot	1.019	2.879	1.031	4.747	1.044	6.662	1.057	8.623
	L/4	1.020	−1.886	1.033	−3.112	1.047	−4.370	1.060	−5.661
	Vault	1.017	4.928	1.028	8.117	1.040	11.377	1.051	14.710
A-2	Gate-side arch foot	1.021	−4.503	1.032	−6.727	1.042	−8.997	1.053	−11.314
	L/4	1.007	6.069	1.011	9.006	1.015	11.965	1.018	14.944
	3L/4	1.011	−2.209	1.016	−3.284	1.022	−4.369	1.027	−5.467

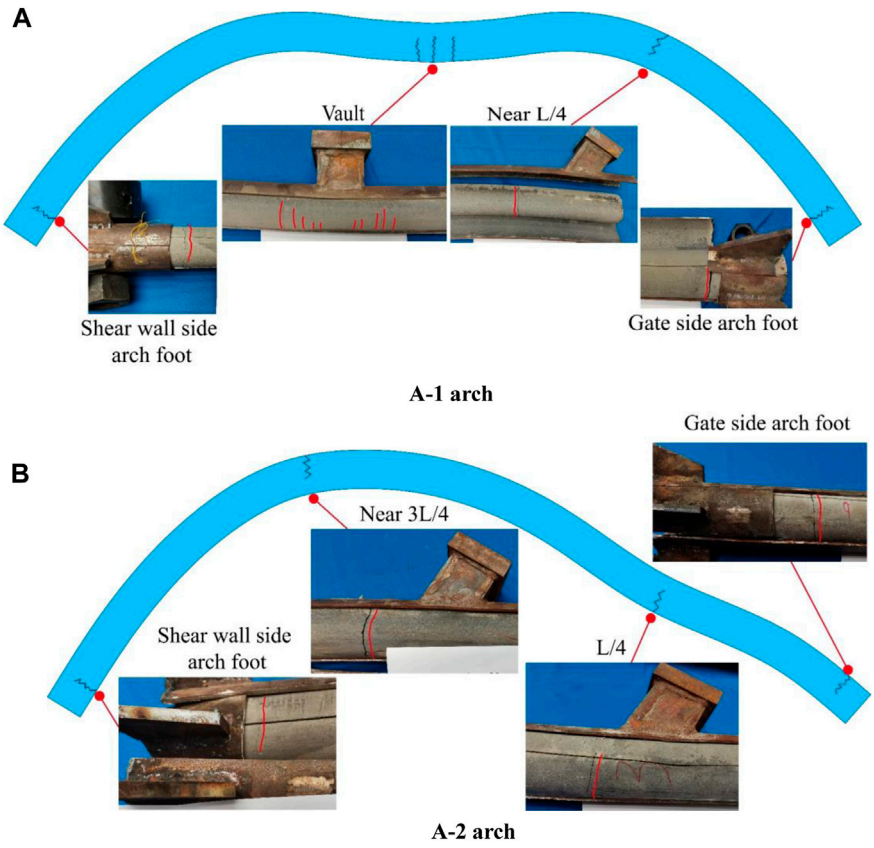

FIGURE 13
Failure state of concrete in the pipe after failure: **(A)** A-1 arch; **(B)** A-2 arch.

TABLE 9 A-1 arch P_1~P_4 measured displacement (unit: mm).

Loading	L/4		Vault	
	δ	ω	δ	ω
P_1	−2.23	−1.89	.00	6.08
P_2	−3.76	−3.16	.00	10.35
P_3	−5.34	−4.47	.00	14.86
P_4	−7.30	−6.13	.00	21.14

TABLE 10 A-2 arch P_1~P_4 measured displacement (unit: mm).

Loading	L/4		3L/4	
	δ	ω	δ	ω
P_1	10.53	12.50	8.14	−9.38
P_2	16.05	19.16	12.39	−14.22
P_3	21.94	26.37	16.82	−19.23
P_4	30.70	37.47	22.50	−25.64

The comparison results show that the results of the two modes at the beginning of the geometric non-linearity of the A-1 and A-2 arches are in good agreement. As the load was increased, the geometric non-linearity has the greatest effect under the critical external load P4 at the end of the elasto-plastic phase. At this time, the measured value of the arch foot section of the A-1 arch is 2.04% larger than the regulation calculation value, the measured value of the L/4 section is about 6.81% larger than the regulation calculation value, and the measured value of the arch top section is about 3.38% smaller than the regulation calculation value. The measured value of the arch foot section of the A-2 arch is about 5.31% larger than the regulation calculated value, the measured value of the L/4 section is about .73% smaller than the regulation calculated value, and the measured value of the 3L/4 section is about 15.73% larger than the regulation calculated value. It shows that the geometric non-linear moment value of the control section of the CFST arch calculated by the eccentricity increase coefficient in the regulation is conservative, but the influence of geometric non-linearity of other sections is not considered enough, and the local damage of other sections may occur before the control section under the action of the large vertical load, which also shows that the calculation mode of the regulation, considering the whole arch affected by geometric non-linearity due to the eccentricity increase coefficient, is not reasonable.

TABLE 11 Measured values of geometric non-linear internal forces (unit: kN m).

Condition	Cross-section position	Internal force	P_1	P_2	P_3	P_4
A-1	Gate-side arch foot	H_A	12.764	20.823	28.917	37.431
		V_A	7.947	12.947	17.948	22.947
		M_A	2.872	4.721	6.615	8.799
	L/4	M_g (L/4)	−1.915	−3.161	−4.444	−6.046
	Vault	M_g (L/2)	4.889	8.048	11.272	14.213
A-2	Cross-section position	H_A	7.976	11.794	15.638	19.796
		V_A	13.946	20.623	27.309	34.1
		M_A	−4.514	−6.774	−.134	-11.915
	L/4	M_g (L/4)	6.098	9.109	12.149	14.835
	3L/4	M_g (3L/4)	−2.321	−3.501	−4.745	−6.327

TABLE 12 Comparison of regulation values and measured values (unit: kN m).

Condition	Cross-section position	Loading	Regulation value	Measured value	Difference ratio (%)
A-1	Gate-side arch foot	P_1	2.88	2.87	−.24
		P_2	4.75	4.72	−.54
		P_3	6.66	6.62	−.70
		P_4	8.62	8.80	2.04
	L/4	P_1	−1.89	−1.92	1.53
		P_2	−3.11	−3.16	1.58
		P_3	−4.37	−4.44	1.69
		P_4	−5.66	−6.05	6.81
	Vault	P_1	4.93	4.89	−.80
		P_2	8.12	8.05	−.85
		P_3	11.38	11.27	−.92
		P_4	14.71	14.21	−3.38
A-2	Gate-side arch foot	P_1	−4.50	−4.51	.23
		P_2	−6.73	−6.77	.69
		P_3	−9.00	−9.13	1.52
		P_4	−11.31	−11.92	5.31
	L/4	P_1	6.07	6.10	.48
		P_2	9.01	9.11	1.14
		P_3	11.96	12.15	1.54
		P_4	14.94	14.84	−.73
	3L/4	P_1	−2.21	−2.32	5.07
		P_2	−3.28	−3.50	6.61
		P_3	−4.37	−4.75	8.60
		P_4	−5.47	−6.33	15.73

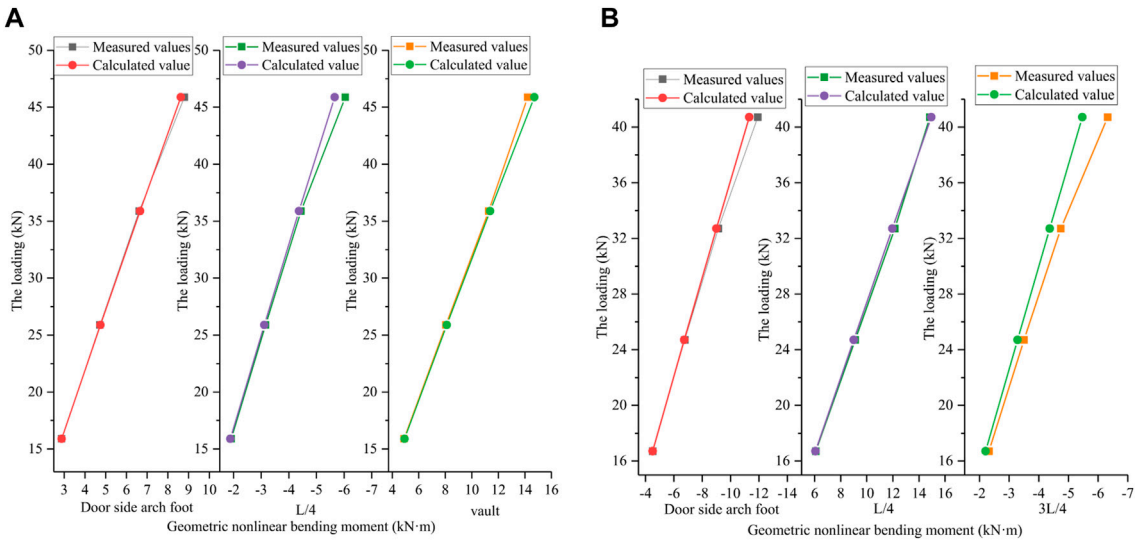

FIGURE 14
Comparison of geometric non-linear bending moment values between the "arch mode" and "rod mode": **(A)** A-1 arch;**(B)** A-2 arch.

5 Conclusion

The specific results of the analysis are as follows:

(1) The failure of the arch mainly comes from the linear bending moment generated by the internal force of the arch foot and the external load and the non-linear bending moment directly generated by the external load after deformation. In contrast, the eccentric compression column mainly comes from the linear bending moment generated by the eccentric force and the non-linear bending moment generated by the transverse deformation or transverse force. These two modes have different force structures, force transmission routes, and deformation sources, which lead to different bearing mechanisms.

(2) The deformation state of the arch in the whole process is divided into three stages: elastic deformation, elastic–plastic deformation, and plastic deformation. Similar to the eccentric compression column, its failure mode is also a hinge failure. However, the experimental phenomenon showed that due to different bearing mechanisms of the two modes, the final failure state of the arch exhibits 4-hinge failure and has strong plastic deformation ability. In contrast, the eccentric compression column exhibits single-hinge failure, which indicates that the deformation ability of the arch is inevitably reduced after the arch is equivalent to a column of considerable length.

(3) The initial geometric non-linear moments measured based on the "arch mode" are in good agreement with the calculated results of the "rod mode." However, the increase in load increased the proportion of geometric non-linear effects, and the geometric non-linear moments calculated by the eccentricity increase coefficient are conservative. In the complex force environment, there is a high possibility of local damage of other sections before the control section, which indicates that the calculation mode of the regulation considering the full arch affected by geometric non-linearity through the eccentricity increase coefficient is not good.

(4) This paper proposes a new calculation model for CFST arch bridges considering geometric non-linear internal forces, which can provide a new idea for the future large-span arch bridge bearing capacity and stability and other verification models. It can help optimize the arch axis and arch rib section form and structure and enhance the arch bridge span.

Data availability statement

The original contributions presented in the study are included in the article/Supplementary Material; further inquiries can be directed to the corresponding author.

Author contributions

SW mainly provided key ideas and insights. YL authored the paper. ZL and TC assisted with the paper.

Funding

This work was supported by Science and Technology Innovation Project of Chongqing Education Commission "Construction of Twin Cities Economic Circle in Chengdu-Chongqing Region" (KJCXZD2020032), Natural Science Foundation of Chongqing (cstc2021jcyj-msxm2491), Guangxi Key Research and Development Program (GuikeAB22036007-8), Chongqing Technology Innovation and Application Development Special Key Project (CSTB2022TIAD-KPX0205). This support is gratefully acknowledged.

Conflict of interest

The authors declare that the research was conducted in the absence of any commercial or financial relationships that could be construed as a potential conflict of interest.

Publisher's note

References

Bradford, M. A., and Pi, Y-L. (2014). Geometric nonlinearity and long-term behavior of crown-pinned CFST arches. *J. Struct. Eng.* 141 (8), 04014190. doi:10.1061/(asce)st.1943-541x.0001163

Chen, B. C. (2016). *Concrete filled steel tube Arch Bridge*. Beijing: People's Communications Publishing House, 276–277. [In Chinese].

Chen, B. C., Qin, Z. B., and Chen, Y. J. (2004). "Equivalent beam and column method for simplified calculation of ultimate bearing capacity of concrete-filled steel tubular arch," in Proceedings of the 16th National Bridge Conference 2, Changsha, China, 9–14. [In Chinese].

Guo, F., Li, P. F., and Mao, J. Y. (2022). Dong yanzhao. Calculation method for increasing coefficient of arch rib eccentricity of long-span arch bridge. *J. Jilin Univ. Eng. Technol. Ed.* 52 (06), 1404–1412. [In Chinese]. doi:10.13229/j.cnki.jdxbgxb20220147

Huo, X. J., and Han, L. Z. (2014). Analysis of geometric nonlinearity of special-shaped arch bridges. *J. Highw. Transp. Res. Dev. Engl. Ed.* 8 (3), 37–45. doi:10.1061/jhtrcq.0000395

Jiang, W., Wang, L., and Li, Y. J. (2018). Out-plane stability safety factors of CFST arches using inverse finite element reliability method. *IOP Conf. Ser. Mater. Sci. Eng.* 392 (2), 022035. doi:10.1088/1757-899X/392/2/022035

Li, J. (2012). *Study on the increase coefficient of bending moment of reinforced concrete arch bridge*. Sichuan, China: Southwest Jiaotong University. [In Chinese].

Li, L., and Lei, K. (2022). Research on influence factors of bearing capacity of concrete-filled steel tubular arch for traffic tunnel. *Symmetry* 14 (1), 167. doi:10.3390/SYM14010167

Lin, S. S., and Chen, B. C. (2016). Calculation of bearing capacity of reinforced concrete arch by equivalent beam-column method. *J. Fuzhou Univ. Nat. Sci. Ed.* 44 (01), 110–114. [In Chinese].

Liu, K. M., and Sun, X. Z. (2021). Bearing capacity of concrete filled steel tube circular arch under the six-point uniformly distributed loading and its engineering application. *Adv. Mater. Sci. Eng.* 2021, 2021–2113. doi:10.1155/2021/8288648

Liu, Y., Wang, D., and Zhu, Y. Z. (2011). Analysis of ultimate load-bearing capacity of long-span CFST arch bridges. *Appl. Mech. Mater.* 1446, 1149–1156. doi:10.4028/www.scientific.net/amm.90-93.1149

Ministry of Transport of the People's Republic of China (2015). *Code for design of concrete filled steel tube arch bridge for highway*. Beijing, China. (JTG/T D65-06-2015) [In Chinese].

Wang, J. Z., and Guo, J. F. (2020). Analysis of influence factors and stability of concrete-filled steel tube arch bridge. *IOP Conf. Ser. Mater. Sci. Eng.* 768 (3), 032053. doi:10.1088/1757-899X/768/3/032053

Wang, W. (2009). "Ultimate capacity analysis of concrete-filled steel tubular structure under eccentric compression," in International Conference on Transportation Engineering, Chengdu, China, 1481–1486.

Wei, J. G., Chen, B. C., and Wu, Q. X. (2010). Equivalent beam-column method for calculation of nonlinear critical Load of concrete-filled steel tube flexural arch. *Eng. Mech.* 27 (10), 104–109. [In Chinese].

Wei, J. G., Chen, B. C., and Wu, Q. X. (2009). Equivalent beam-column method for calculation of ultimate bearing capacity of bending steel pipe. *Chin. J. Comput. Mech.* 26 (01), 87–93. [In Chinese].

Wu, X. R., Liu, C. Y., Wang, W., and Wang, Y. Y. (2015). In-plane strength and design of fixed concrete-filled steel tubular parabolic arches. *J. Bridge Eng.* 20 (12). doi:10.1061/(ASCE)BE.1943-5592.0000766

Yang, L. F., Xie, W. W., Zhao, Y. F., and Zheng, J. (2020). Linear elastic iteration technique for ultimate bearing capacity of circular CFST arches. *J. Constr. Steel Res.* 172, 106135. doi:10.1016/j.jcsr.2020.106135

Ye, S. (2013). Parameter analysis on ultimate load-carrying capacity of CFST arch rib with new-type dumbbell-shaped section. *Adv. Mater. Res.* 2203, 634–638. doi:10.4028/www.scientific.net/AMR.634-638.3825

Yuan, C. C., Hu, Q., Wang, Y. Y., and Liu, C. (2020). Out-of-plane stability of fixed concrete-filled steel tubular arches under uniformly distributed loads. *Mag. Concr. Res.* 73 (18), 945–957. doi:10.1680/jmacr.19.00526

Zhang, Y. F., Guo, D. L., and Mei, B. R. (2022). Numerical analysis of eccentric compression performance of CFRP-confined concrete-filled steel tube (CFST) columns. *J. Institution Eng. (India) Ser. A* 103 (2), 543–555. doi:10.1007/S40030-022-00638-0

Zhang, Y. Y., and Yu, C. L. (2013). Nonlinear stability impact of concrete-filled steel tube arch bridge. *Adv. Mater. Res.* 2605, 1168–1171. doi:10.4028/www.scientific.net/amr.785-786.1168

Zhao, Y. F., Xie, W. W., and Yang, L. F. (2021). Elastic modulus reduction method for stable bearing capacity analysis of dumbbell-shaped CFST arches. *J. Phys. Conf. Ser.* 2044 (1), 012163. doi:10.1088/1742-6596/2044/1/012163

Zou, Y., Yu, K., Heng, J., Zhang, Z., Peng, H., Wu, C., et al. (2023). Feasibility study of new GFRP grid web - concrete composite beam. *Compos Struct.* 305, 116527. doi:10.1016/j.compstruct.2022.116527

Zou, Y., Zheng, K. D., Zhou, Z. X., Zhang, Z. Y., Guo, J. C., and Jiang, J. L. (2023). Experimental study on flexural behavior of hollow steel-UHPC composite bridge deck[J]. *Eng. Struct.* 274, 115087. doi:10.1016/j.engstruct.2022.115087